Gaseous "nanoprobes" for detecting gas-trapping environments in macroscopic films of vapor-deposited amorphous ice

Sukhpreet K. Talewar, Siriney O. Halukeerthi, Regina Riedlaicher (iD), Jacob J. Shephard, Alexander E. Clout, Alexander Rosu-Finsen, Gareth R. Williams, Arne Langhoff, Diethelm Johannsmann, and Christoph G. Salzmann (iD)

View Online   Export Citation   CrossMark

ARTICLES YOU MAY BE INTERESTED IN

Gaseous "nanoprobes" for detecting gas-trapping environments in macroscopic films of vapor-deposited amorphous ice

Sukhpreet K. Talewar,[1] Siriney O. Halukeerthi,[1] Regina Riedlaicher,[1] [iD] Jacob J. Shephard,[1]
Alexander E. Clout,[1,2] Alexander Rosu-Finsen,[1] Gareth R. Williams,[2] Arne Langhoff,[3]
Diethelm Johannsmann,[3] and Christoph G. Salzmann[1,a)] [iD]

AFFILIATIONS

[1] Department of Chemistry, University College London, 20 Gordon Street, London WC1H 0AJ, United Kingdom
[2] UCL School of Pharmacy, University College London, 29-39 Brunswick Square, London WC1N 1AX, United Kingdom
[3] Institute of Physical Chemistry, Clausthal University of Technology, Arnold-Sommerfeld-Str. 4, Clausthal-Zellerfeld, Germany

[a)] E-mail: c.salzmann@ucl.ac.uk

ABSTRACT

Vapor-deposited amorphous ice, traditionally called amorphous solid water (ASW), is one of the most abundant materials in the universe and a prototypical material for studying physical vapor-deposition processes. Its complex nature arises from a strong tendency to form porous structures combined with complicated glass transition, relaxation, and desorption behavior. To gain further insights into the various gas-trapping environments that exist in ASW and hence its morphology, films in the 25–100 μm thickness range were codeposited with small amounts of gaseous "nanoprobes" including argon, methane, helium, and carbon dioxide. Upon heating in the 95–185 K temperature range, three distinct desorption processes are observed which we attribute to the gas desorption out of open cracks above 100 K, from internal voids that collapse due to the glass transition at ~125 K and finally from fully matrix-isolated gas induced by the irreversible crystallization to stacking disordered ice (ice Isd) at ~155 K. Nanoscale films of ASW have only displayed the latter desorption process which means that the first two desorption processes arise from the macroscopic dimensions of our ASW films. Baffling the flow of water vapor toward the deposition plate greatly reduces the first desorption feature, and hence the formation of cracks, but it significantly increases the amount of matrix-isolated gas. The complex nature in which ASW can trap gaseous species is thought to be relevant for a range of cosmological processes.

Published under license by AIP Publishing. https://doi.org/10.1063/1.5113505

INTRODUCTION

Water displays tremendous structural diversity in its solid forms including 18 crystalline phases of ice[1,2] and at least two distinct amorphous forms.[3–6] As one of the most abundant molecules in the universe, H_2O has been detected on interstellar dust grains, comets, and large bodies such as planets and moons.[7–10] In the dark molecular clouds of the interstellar medium, H_2O mantles on grains are predominantly formed by reactive accretion of H and O atoms as the temperature approaches 10 K in the cores of the molecular clouds.[7,8,11] In the lab, interstellar ice analogs are commonly made by vapor deposition onto a cold surface in a vacuum.[12–14] In the 15–30 K range, vapor-deposited H_2O forms a high-density amorphous ice which converts to low-density amorphous (LDA) ice upon heating above 80 K.[14–16] However, it is emphasized that the denser low-temperature amorphous ice should not be confused with the high-density amorphous ice obtained upon pressure-amorphization of ice I.[3] Traditionally, amorphous ice obtained by vapor deposition has been labeled "amorphous solid water" (ASW).[17,18] In addition to its widespread occurrence in space, ASW may also form in the coldest regions of the Earth's atmosphere where the temperatures drop below 150 K.[19]

The local structure of ASW is very similar compared to other forms of LDA.[20] However, a defining feature of ASW is that it can display highly porous structures.[21–23] The exact experimental details of the cryogenic vapor-deposition can have pronounced effects on the morphologies of the ASW deposits. A wide range of factors are important including the baffling of the water-vapor beam,

substrate temperature, overall flux, impingement energy, film thickness, and deposition angle.[14,21,24–27] Upon heating in vacuum, the pores collapse in the 120–140 K range. If the pores are filled with gases before the collapse, then the formation of clathrate hydrates can be observed upon heating.[28] During the sintering process, the dangling O–H groups at the surface of the pores are removed according to dielectric[29] and Raman spectroscopy.[30] Using Raman and FTIR spectroscopy, it has also been shown that a gradual structural relaxation process takes place upon heating ASW from a ~95 K deposition temperature to the irreversible crystallization to stacking disordered ice I (ice Isd) at ~150 K.[31]

Like other forms of LDA, ASW displays a weak endothermic glass transition in calorimetry at ~137 K.[32,33] However, it is important to note that as-deposited samples only show exothermic relaxation effects upon heating, reflecting the highly unrelaxed nature of the vapor-deposited material. The glass transition with a small stepwise increase in heat capacity only becomes observable after prolonged annealing at 130 K.[33] The mechanism of the glass transition of LDA is still debated.[31,34–40] However, it seems likely that the collapse of pores upon heating is connected with the underlying process that leads to an endothermic increase in heat capacity. The translational component of the sintering process should thereby not be taken as evidence for a transition to a supercooled liquid since it may merely reflect the unrelaxed state of the starting material.[37] Furthermore, translational motion may be caused by the increased vapor pressure of ASW at temperatures around its glass transition.[41] In summary, ASW is a highly complex material both from the structural as well as dynamic perspective. Further insights into its properties will not only lead to a better understanding of its role in important cosmological processes but will also be important for our understanding of the cryogenic physical vapor deposition of other materials.[42]

In the present work, small amounts of gaseous "nanoprobes" are codeposited with ASW to investigate the existence of different "trapping" environments. This is probed by following desorption processes with mass spectroscopy upon heating the deposits in the 95–185 K temperature range. In contrast to related studies of nanoscale ASW films,[43–46] macroscopic films of ASW are prepared on a large deposition plate on the gram scale. A detailed understanding of the various trapping environments is obtained by using several different gases with different physical properties including argon, methane, helium, and carbon dioxide. Furthermore, we investigate the effects of film thickness, deposition rate, and baffling the flow of the water vapor toward the deposition plate on the desorption properties of argon. Since the exact details of the deposition conditions are very important for the morphology of ASW, we use a quartz-crystal microbalance (QCM) to "map" the shape of the vapor beam entering the vacuum chamber. The potential of using QCM measurements for detecting changes in the viscoelastic properties of the deposits upon heating is also explored.

EXPERIMENTAL METHODS

Experimental setup for cryogenic physical vapor deposition

A schematic illustration of the experimental setup is shown in Fig. 1(a). The main body is a Kurt Lesker high-vacuum stainless steel
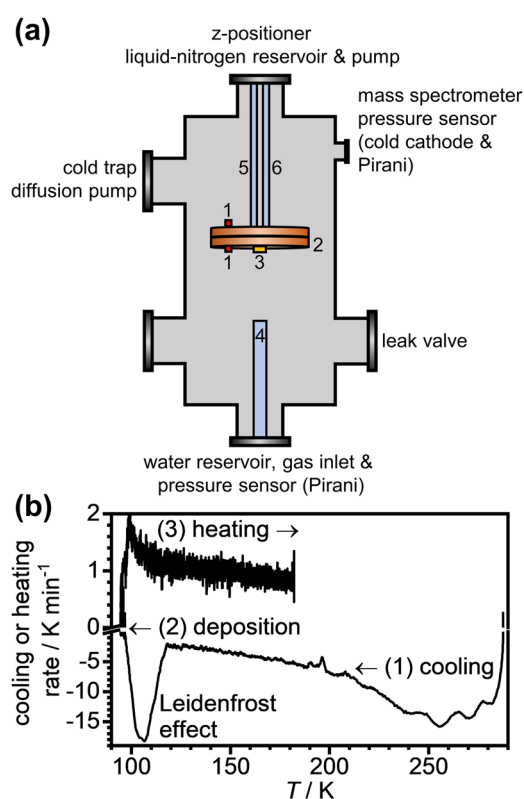

FIG. 1. (a) Schematic illustration of the experimental setup for cryogenic vapor deposition. A range of accessories are connected to the ports of the vacuum chamber as indicated. The components inside the chamber are (1) K-type thermocouple temperature sensors, (2) removable cryogenic deposition plate, (3) quartz crystal microbalance sensor, (4) inlet tube for water vapor/gases, (5) feedthrough connected to a liquid nitrogen reservoir, and (6) feedthrough connected to a rotary-vane pump. (b) Cooling/heating rates during a typical experiment.

box chamber with internal dimensions of 12 in. × 12 in. × 24 in. equipped with a range of KF-40 and ISO-K 100 ports. Access to the chamber is gained through a large aluminum front door with a glass viewing window. A double-stage rotary-vane pump (model 12, BOC Edwards) is used to achieve a rough vacuum and to back a diffusion pump (Diffstak 63/150M, BOC Edwards) achieving a base pressure of $<2 \times 10^{-6}$ mbar as measured by a combination cold cathode/Pirani pressure gauge (PenningVac PTR 90, Oerlikon Leybold Vacuum). A liquid-nitrogen cold trap is situated above the diffusion pump trapping ice and oil residues.

Inside the vacuum chamber, a circular 8 in.-diameter copper plate is suspended using two feedthrough tubes connected to a liquid-nitrogen reservoir on one side and to a single-stage rotary-vane pump (Sogevac SV16, Oerlikon Leybold Vacuum) on the other side. To achieve maximal cooling of the plate, the two feedthroughs are connected to a spiral-shaped copper tubing soldered onto the copper plate. Using a linear z-positioner, the vertical position of the cryogenic plate can be changed over a travel distance of 25 cm inside the chamber. A second 8 in.-diameter copper plate can be attached to the first plate with screws so that it can be removed from the

chamber after sample deposition, while keeping the plate immersed in liquid nitrogen. The temperatures of both plates were measured using K-type thermocouples connected to an IJ-6 software-based temperature controller. Using maximal suction from the single-stage rotary-vane pump, a base temperature of 95 K can be reached for both copper plates. The cooling rates achieved in a typical experiment are shown in Fig. 1(b). The pronounced increase in the cooling rate below ~120 K is due to the Leidenfrost effect as the cold nitrogen gas starts to wet the surfaces inside the cooling system.

At the bottom of the vacuum chamber, a 32 cm long and 2.6 cm wide stainless steel tube leaks water vapor mixed with additional gases if needed into the chamber. The inlet system consists of two needle valves (EV 016 DOS AB, Oerlikon Leybold Vacuum) controlling the inlet of water vapor and other gases as well as a Pirani pressure sensor (Thermovac TTR91, Oerlikon Leybold Vacuum). A round-bottom glass flask fitted with a Young's tap containing ultra-pure water (H_2O, Milli-Q, Millipore) is attached to the first needle valve. Before a deposition experiment, the water was degassed three times using the freeze-pump-thaw method. The round-bottom flask can be removed from the system after an experiment to weigh the amount of water leaked into the chamber. The second needle valve is connected to a gas reservoir which is flushed with gas from a commercial gas cylinder. Since the pressure difference at this inlet is close to 1 bar, the high-accuracy graduated needle valve can be used to leak defined amounts of gas into the vacuum chamber in mmol s^{-1} using a chart provided by the manufacturer (cf. Fig. S1). Argon (99.998%), methane (99.995%), carbon dioxide (99.8%), and helium gas (99.995%) were purchased from BOC Ltd. and used as received.

To baffle the flow of gas into the chamber, an iron mesh with 0.5 mm thick wires spaced 1 mm apart was placed directly on top of the inlet tube. For complete disruption of the gas flow, the mesh was raised by 1 cm and a two-pence coin, which matches the diameter of the inlet tube, was placed on top.

Cryogenic deposition experiments

At a base pressure below 2×10^{-6} mbar and a temperature of the deposition plate of ~95 K, water vapor was leaked into the chamber. The leak rate was adjusted with the needle valve by setting the inlet pressure to 0.100 mbar. This led to an only slight pressure increase on the back side of the deposition plate into the low 10^{-5} mbar range, illustrating the effective cryogenic action of the deposition plate. Additional gases were mixed into the flow of water vapor by selecting the desired leak rates on the second leak valve. The deposition time for a typical experiment was 2 h during which ~1.5 g of water entered the vacuum chamber. Unless stated otherwise, a gas leak rate of 1.35×10^{-5} mmol s^{-1} was used.

Quartz-crystal microbalance (QCM) measurements

Gold-plated AT-cut 6 MHz planoconvex quartz crystals (Sycon Instruments) were placed inside an Allectra 710-SH sensor firmly attached onto the deposition plate. The QCM sensor was connected to a reflection bridge and a 0.5–60 MHz N2PK vector network analyzer through coaxial cables. The deposition rates were monitored by recording the changes in the fundamental resonance frequency in the electrical conductance data over time using the myVNA and QTZ softwares.

For mapping the shape of the water vapor flow into the chamber, the QCM sensor was positioned at different locations on the deposition plate and the vertical position was changed with the z-positioner. The local deposition rates were determined by calculating the derivatives of the recorded frequencies with respect to time.

Temperature-programmed desorption (TPD) experiments

Following the two-hour deposition, the deposition plate was kept at ~95 K for 1 h to allow the vacuum system to reach base pressure again. A residual gas analyzer mass-spectrometer (RGA-MS, Hiden Analytical, HALO 201) equipped with a Faraday cup was then set to continuously record partial pressures in the 1–50 m/z mass range, while the deposition plate was allowed to warm to ~185 K. At this temperature, the total pressure reached 1×10^{-4} mbar which is the upper limit for the Faraday cup. Upon heating from 95 to 185 K, the heating rate changed from ~1.7 K min^{-1} at 100 K to ~0.8 K min^{-1} at 185 K as shown in Fig. 1(b).

Ex situ x-ray diffraction of the deposited material

Following deposition, the ASW deposit was annealed at 125 K under vacuum and cooled back to 95 K. This step was necessary to prevent the formation of nitrogen clathrate hydrate which forms when highly porous as-made ASW is exposed to liquid nitrogen.[28] The chamber was then vented to atmospheric pressure with cold and dry nitrogen gas from a liquid nitrogen reservoir through a gate valve (series 012 mini gate valve, VATvalve). The deposition plate was then quickly submerged in liquid nitrogen, detached from the cryostat and removed from the chamber. The deposited material on the sample plate was scraped off the deposition plate and transferred into a purpose-built Kapton-window sample holder under liquid nitrogen. X-ray diffraction patterns were collected using a Stoe Stadi P X-ray diffractometer (Cu Kα1 radiation at 40 kV, 30 mA and monochromated by a Ge 111 crystal) equipped with a Mythen 1 K linear detector. The temperature of the samples was maintained at 95 K with an Oxford Instruments CryojetHT.

RESULTS AND DISCUSSION
Shape of the water-vapor beam entering the vacuum chamber

As mentioned earlier, the exact experimental details of the cryogenic vapor-deposition have pronounced effects on the morphologies of ASW deposits.[14,21,24–27] In a first step, we therefore characterized the deposition conditions in our vacuum chamber, which, compared to other setups, contains a very large cryogenic deposition plate with an area of 324 cm^2. The large plate enables the preparation of ASW on the gram scale. But it also means that the deposition rates may not necessarily be uniform across the entire plate.

To determine the local deposition rates within the vacuum chamber, the QCM sensor was positioned at different locations on the plate and the vertical position of the plate within the chamber was changed with the z-positioner. Since H_2O has a very

high sticking probability at 77 K, these experiments enabled us to effectively "map" the shape of the water-vapor beam within the vacuum chamber.

According to the Sauerbrey equation, a linear relationship with a negative constant of proportionality exists between the resonance frequency of a quartz crystal and the deposited mass.[47,48] This means that the frequency of the oscillator decreases during a deposition experiment. The deposition rate can then be estimated from the derivative of the quartz frequency with respect to time. The local deposition rates within the vacuum chamber are shown in Fig. 2. These were determined by leaving the flow of water vapor into the chamber unperturbed, baffled with an iron mesh and blocked with a two-pence coin above the inlet tube.

As expected, the water-vapor beam displays a strong directionality as it enters the vacuum chamber without baffling [Fig. 2(a)]. Further away from the inlet tube, the beam becomes more diffuse. Yet, even at 22 cm away from the inlet tube, the deposition profile across the plate is still far from uniform. Using an iron mesh on the inlet tube renders the beam more diffuse at larger deposition distances as shown in Fig. 2(b), indicating some degrees of beam perturbation. Placing a solid metal disk directly above the inlet tube leads to a drastic change in the beam shape, as can be seen in Fig. 2(c). At lower distances, the largest deposition rates are found at the edges of the deposition plate presumably caused by the "reflection" of the beam from the walls of the vacuum chamber. Interestingly, at larger distances, the fastest deposition is found at the center of the deposition plate. It can be speculated that this could be due to a second "bounce" of the beam from the walls of the chamber. At the center of the deposition plate and a deposition distance of 15 cm, the deposition rate decreases from 0.724 to 0.472 and 0.316 μg cm^{-2} s^{-1} as the
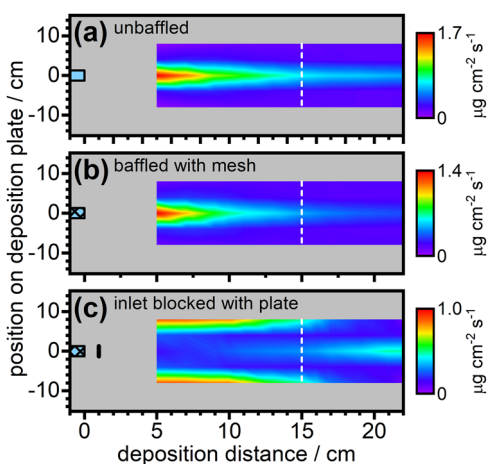

FIG. 2. "Mapping" of the shape of the H$_2$O vapor beam inside the vacuum chamber using QCM measurements for (a) unperturbed flow, (b) flow baffled with a mesh, and (c) blocking of the flow with a plate. The local deposition rates are shown as contour plots plotted against the deposition distance and the position on the deposition plate. The gray areas correspond to the parts of the vacuum chamber where the depositions rates could not be determined [cf. Fig. 1(a)]. The white dashed lines indicate the chosen distance of 15 cm used for the following deposition experiments. Cross sections through the contour plots are shown in Fig. S4.

unbaffled flow is restricted by the mesh and plate, respectively (cf. Fig. S4).

On the basis of these experiments, it was decided to use the mesh for baffling as well as a deposition distance of 15 cm for the following experiments. These conditions seem to be a reasonable compromise in terms of achieving a uniform film thickness across the deposition plate, while at the same time not sacrificing the overall deposition yield. Judging from the very small increases in pressure on the backside of the deposition plate during deposition with the mesh (cf. section titled "Experimental methods") and the shape of the beam at 15 cm, it can be assumed that the water vapor leaked into the chamber is deposited almost quantitatively on the plate. Consistent with this, the liquid nitrogen-cooled parts on the down-stream side of the deposition plate did not show any ice deposit after the deposition experiments, whereas "milky" white films were clearly visible on the deposition plate.

Preparation and thermal characteristics of pure ASW films

The amorphous nature of a deposit after a two-hour deposition experiment was confirmed by recovering the deposition plate from the chamber under liquid nitrogen and *ex situ* analysis of the deposit with X-ray diffraction. At 95 K, the sample displayed the characteristic broad diffraction features of ASW with the first strong diffraction peak centered at ~24°, as shown in Fig. 3(a).[12,33,49] Upon heating, the ASW transformed to stacking-disordered ice, ice Isd, starting at around 140 K.[32,49–51]

Figure 3(b) shows the changes in the fundamental quartz-oscillator frequency during a typical deposition experiment followed by heating in vacuum. As expected, the frequency decreases during the deposition and it does so by more than 500 kHz, which is rather exceptional. In most other instances, films of similar thickness overdamp the resonance.[52] Given the large frequency change, some common artifacts (for instance, caused by temperature) can be ignored.

Before the deposition starts, the quartz crystal resonates at 5.972 MHz which decreases to 5.454 MHz after the two-hour deposition. Considering the large frequency shift, the Sauerbrey equation, which is typically used to derive a mass per unit area from a frequency shift, is only an approximation.[53] The reason is the large frequency shift itself and, also, a possible influence of viscoelastic effects which come into play when the film thickness is a sizeable fraction of the wavelength of the shear sound. With the limitations of the Sauerbrey equation acknowledged, we still proceed with an estimate of the mass per unit area. Using the known conversion constants (~−5.7 Hz nm^{-1} at a density of ρ = 1 g cm^{-3}), Δf = −518 kHz corresponds to a mass of 9050 μg cm^{-2}. Converting this number to a film thickness requires an assumption on the density which is poorly known because of porosity. Using $\rho \approx 0.93$ g cm^{-3} as a bulk density of low-density amorphous ice,[54] a thickness around 100 μm is obtained. Considering the porosity of ASW,[22,23,26] the actual thickness of the deposited ASW film is likely to be greater.

Upon heating the ASW film, an increase in the frequency is detected in the QCM frequency starting at 130 K. At the same time, the vapor pressure increases, as shown in Fig. 3(c), which points toward a mass loss as the reason for the frequency increase.
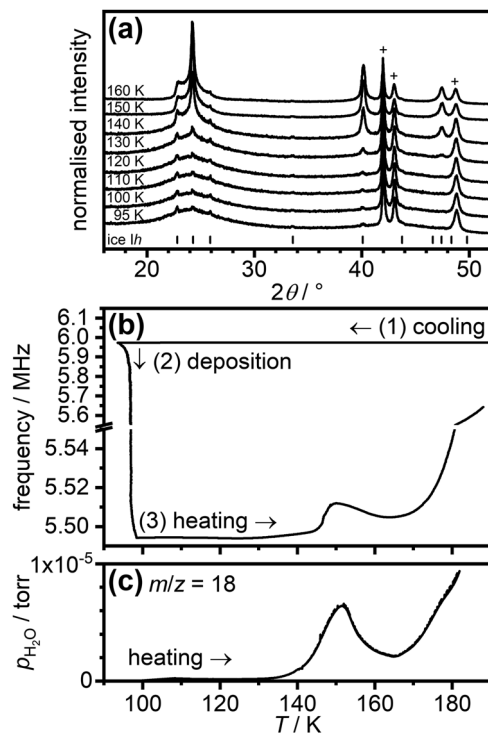
FIG. 3. Preparation and thermal characteristics of pure ASW. (a) *Ex situ* X-ray diffraction patterns of recovered ASW recorded upon heating from 95 to 160 K. Bragg peaks due to the brass sample holder are highlighted with crosses and tick marks show the expected positions of Bragg peaks of ice I*h*. The small amounts of ice I*h* present in the initial sample are due to vapor condensation during the sample transfer. (b) Frequency changes in the fundamental QCM frequency recorded (1) upon cooling, (2) during deposition at ~95 K, and (3) upon heating with the sensor at the center of the deposition plate and 15 cm away from the inlet tube. (c) Partial pressure of water (*m/z* = 18) upon heating ASW.

However, both viscoelastic effects and release of bending stress may contribute here as well. Such effects may also be responsible for the unusual frequency decreases above 150 K. A detailed analysis and discussion of the QCM data is presented in the supplementary material. At 170 K, the frequency begins to rise again which is most likely due to the desorption of ice I*sd* as its vapor pressure increases with temperature.

The sequence of phase changes can also be observed from the changes in the partial pressure of water recorded with the mass spectrometer upon heating, as shown in Fig. 3(c). A first maximum in the vapor pressure can be seen at around 150 K, which is followed by a decrease as the sample has transformed from ASW to ice I*sd*. Since ASW is higher in free energy than in ice I*sd*, it is expected to display a greater vapor pressure.[18,55,56] The rise in vapor pressure above 170 K is then due to the increasing vapor pressure of ice I*sd* with temperature. According to the QCM data in Fig. 3(b), about half of the deposited film has evaporated at around 190 K. Similar trends in the vapor pressures have also been observed upon heating pure nanoscale ASW films.[18,55] Yet, for thinner films, the temperature-programmed desorption (TPD) experiments typically end with complete desorption.

Desorption of gaseous "nanoprobes" from ASW

Having established the optimal deposition conditions and the TPD behavior of pure ASW films for our setup, water vapor was codeposited with argon gas for 2 h. Compared to the 0.0116 mmol s^{-1} flow of water vapor into the chamber, a very small flow of 1.34 × 10^{-5} mmol s^{-1} argon was mixed into the water beam corresponding to a 1:860 ratio. Since argon is much more volatile than water, the actual amount of argon in the ASW deposit is likely to be much smaller. In fact, we could not detect any systematic trends in the QCM measurements that would suggest argon incorporation. This small amount of argon therefore justifies its use as a "nanoprobe" to detect the different ways in which macroscopic films of ASW can trap gas molecules without altering the properties of the ASW itself. A detailed quantitative analysis will be presented later.

The TPD data of Ar@ASW is shown in Fig. 4(a). In addition to the previously observed trend in the H$_2$O vapor pressure, three distinct argon desorption processes were observed using the mass spectrometer. The first starting at 100 K is quite broad and followed by a slightly sharper desorption feature at ~125 K. The third desorption feature at ~155 K is the most intense and coincides with the H$_2$O desorption peak associated with the crystallization of ASW. Due to the low levels of argon in the deposit, neither of these desorption processes could be detected in the QCM data. It is also noted that the presence of argon did not change the desorption properties of H$_2$O which again justifies its use as a "nanoprobe."

The observation of three distinct argon desorption features in the 95–185 K temperature range is significant. In previous studies, several hundred monolayers of ASW were deposited on top of one monolayer of argon.[43,44] Such deposits only displayed a strong argon desorption peak associated with crystallization and a weak feature at higher temperatures as the entire film evaporated. In analogy to
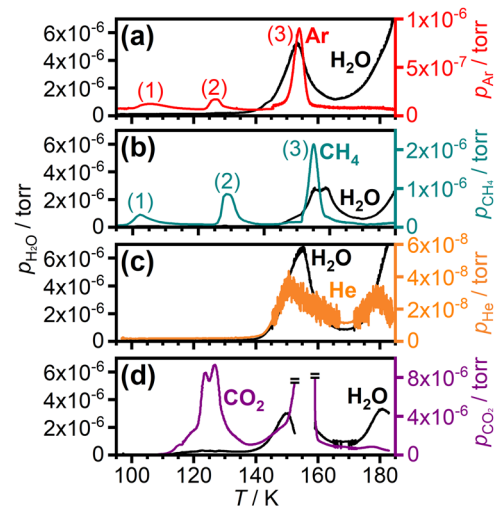
FIG. 4. Partial pressures of water (*m/z* = 18) and various gaseous "nanoprobes" recorded upon heating codeposited ASW films. The codeposited gases are (a) argon (*m/z* = 40), (b) methane (*m/z* = 16), (c) helium (*m/z* = 4), and (d) carbon dioxide (*m/z* = 44). Three distinct desorption processes are highlighted in (a) and (b). In panel (d), the mass spectrometer had to be switched off in the 150–160 K range due to the partial pressures exceeding the upper working limit.

a previous study using CCl_4, the crystallization-induced desorption was described as a "molecular volcano."[57] For comparison, argon deposited on top of ASW already desorbs at temperatures below 50 K.[43,58] For a 100 nm thick ASW film codeposited with argon, only the desorption peak due to crystallization could be observed[45] even when a 1:1 ratio of Ar:H_2O was used for the deposition.[46] Upon heating quite argon-rich mixtures of argon and ASW deposited at 20 K, seven overlapping desorption processes were observed with desorption rates differing by several orders of magnitude.[59] It seems possible that the formation of solid argon in those experiments may have had an influence on the morphology of the ASW. In any case, due to the small amounts of argon used in our study, it is emphasized that we could achieve the baseline separation of the three distinct desorption processes.

As described in the supplementary material, the high-accuracy graduated needle valve was used to calibrate the mass spectrometer so that the measured partial pressures of argon could be converted into desorption rates in mmol s^{-1}. Using the calibration curve shown in Fig. S2, the partial pressures from Fig. 4(a) were converted into desorption rates, as shown in Fig. S3(a). If the desorption rates are plotted against time, then the amounts of released argon from the three desorption features can be obtained by integration. The results from the quantitative analyses of all TPD traces obtained in this study are summarized in Table S1.

Summing over all three desorption features shown in Fig. S3(a), the total release of argon upon heating is 7.127×10^{-5} mmol. This means that only 0.07% of the leaked gas is incorporated within the ASW films which corresponds to a water to argon ratio of 1 169 000:1 in the deposit. The fact that there are more than one million water molecules present for each argon atom now quantitatively underpins our approach to use argon as a gaseous nanoprobe.

Since the desorption processes labeled with (1) and (2) in Fig. 4(a) are absent for nanoscale Ar@ASW,[43–46] they must be due to desorption processes originating from trapping environments that only exist in macroscopic ASW films. As shown schematically in Fig. 5, the desorption features are attributed to three different local environments of argon in ASW. Desorption process (1) is suggested to originate from argon trapped in narrow cracks open to the vacuum. Consistent with this, scanning electron microscopy has recently shown that ASW displays a "cauliflower"-type morphology
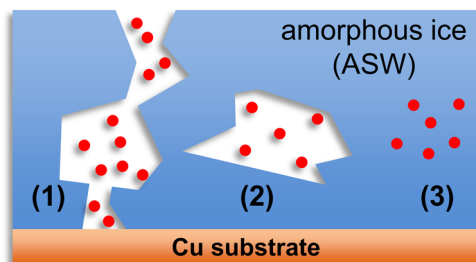

FIG. 5. Schematic illustration of the different possibilities of incorporating argon into ASW films including (1) open cracks, (2) internal voids, and (3) fully matrix isolated gas molecules. The numbering in this schematic corresponds to the labeling of the desorption processes in Fig. 4(a).

with void-separated tapered columns.[60,61] It has also recently been argued that cracks appear in ASW once a critical microscopic film thickness is reached.[62]

The collapse of internal voids due to the onset of the orientational glass transition and subsequent sintering is proposed to lead to desorption feature (2). This process is consistent with the observed changes in low-angle neutron diffraction.[63] Process (3), which coincides with the crystallization of ASW to ice Isd, should then originate from the liberation of fully matrix-isolated argon as it has also been observed for nanoscale Ar@ASW.[43,45] It seems possible that the argon is trapped inside cages within the ASW similar to those observed in clathrate hydrates.

To probe if the open cracks in ASW can be filled after the deposition, a pure film was "bombarded" with argon for 2 h using the "standard" argon flow of 1.34×10^{-5} mmol s^{-1} and heated straight away. The corresponding TPD trace is shown in Fig. S8. Compared to the previous codeposition experiment, the amount of argon released during the first desorption feature is about twice as large, illustrating that the open cracks are accessible and can be filled with argon after the deposition (cf. Table S1). The desorption features at higher temperatures, including an additional weak pre-crystallization feature just below 140 K, release only ~15% of the argon compared to the corresponding features in the codeposition experiment. These weak features are thought to originate from a small fraction of argon initially located in the open cracks which becomes trapped in other environments as the sample is heated. In Refs. 64 and 65, nitrogen gas was adsorbed onto ASW films at 27 K with thicknesses of up to 9 μm. Upon heating, it was found that the nitrogen desorbs at increasingly higher temperatures as the thickness of the films increases. Above 3000 monolayers, the desorption feature started to deviate from a single peak and became more complex with a tail extending beyond 75 K. It is possible that our first desorption feature is related to this process but shifted to even higher temperatures due to the thicknesses of our ASW films. In this sense, the delayed desorption of argon from thick films is due to the enhanced confinement of argon within long, narrow, and tortuous cracks.

To further test the assignments of the desorption features to the various trapping environments, additional gaseous nanoprobes were incorporated into ASW including methane, helium, and carbon dioxide which were leaked into the water-vapor beam at the same leak rates as the argon, therefore maintaining the 1:860 ratio in the beam entering the vacuum chamber. The TPD data of CH_4@ASW also display the three distinct desorption processes, as shown in Fig. 4(b), which means that CH_4 can also be trapped in the three different environments shown in Fig. 5. Compared to Ar@ASW, desorption features (2) and (3) are shifted toward slightly higher temperatures for CH_4@ASW, suggesting somewhat stronger van-der-Waals interactions with the ASW. This is confirmed from the quantitative analysis shown in Fig. S3(b) and the data in Table S1. Upon changing from argon to methane at otherwise identical deposition conditions, the percentage of the gas captured in ASW increases from 0.07% to 0.75% which means that the resulting concentration of methane in ASW is 10 times greater compared to argon.

In contrast to this, helium appears to be too mobile to be trapped in ASW[66] above 95 K, as illustrated in Fig. 4(c). The very weak increases in the helium partial pressure in the temperature

ranges where water desorbs are thought to be linked to the water desorption. As the vacuum pump removes the increasing levels of H_2O gas, slight increases in the helium partial pressures are caused by the increase in the total pressure. In the case of $CO_2@ASW$, the first desorption process is not clearly observed which is attributed to the low volatility of CO_2 compared to the other gases.[67] Given the broadness of the desorption feature at higher temperature, it seems possible that process (1) is simply delayed in case of CO_2 and overlaps with process (2). Again, in case of nanoscale $CO_2@ASW$, only desorption peaks associated with crystallization have been observed.[68] For CO_2-rich ASW mixtures, it has been shown that the CO_2 is quite mobile within the ASW which can lead to low-temperature desorption features[69,70] and even segregation of the CO_2.[71] It is possible that such effects may contribute to our TPD data as well.

In the following, due to its weak interaction with ASW, argon will be used exclusively to probe the effects of changing the experimental deposition conditions on the three desorption features.

Effect of film thickness and deposition rate on the three desorption features

The effect of reducing the deposition time and hence the film thickness on the three desorption features was investigated next while keeping the leak rates of water and argon unchanged. Specifically, the deposition time was reduced from 2 h to 60 and 30 min. Ignoring the porosity of ASW, these films display nominal thicknesses of 50 and 25 μm, respectively. The corresponding TPD traces are presented in Fig. 6(a) which show that the three desorption features are observed independent of the film thickness. The quantitative analysis in Fig. 6(c) shows that the amounts of argon released during the three desorption processes scale in a linear fashion with the deposition time. This means that the morphology and hence the structural characteristics of the various gas-trapping environments in the ASW films do not change as the film thickness is reduced from 100 to 25 μm. Bu et al. argued that macroscopic cracks in ASW start to appear in the 1–5 μm thickness range.[62] In principle, the first desorption feature should not be observed in the absence of cracks. However, due to the experimental constraints of our study and setup (i.e., the water to argon ratio, the heating rate, and the base pressure of the vacuum system), this thickness regime is not easily accessed.

In the next step, the deposition times were kept constant at 2 h, but the leak rates of water and argon were reduced by 50% and 25% from the original rates of 1.157×10^{-2} and 1.345×10^{-5} mmol s^{-1}, respectively, thereby keeping the water to argon ratio constant. The recorded TPD traces are shown in Fig. 6(b), and the quantitative analysis of the three desorption features is shown in Fig. 6(d). In contrast to the dependence on film thickness, decreasing the deposition rates was found to lead to an exponential decrease in the amounts of trapped argon for all three desorption features. These findings could imply that the deposition rate has an influence on the morphology of the resulting ASW films as found in earlier studies.[14,21,24–27] However, in the context of our experiments, kinetic effects of the water molecules trapping the argon may be important as well. The question is essentially how quickly a specific trapping environment is created by the water molecules. Using a lower water deposition rate, even when the argon leak rate is
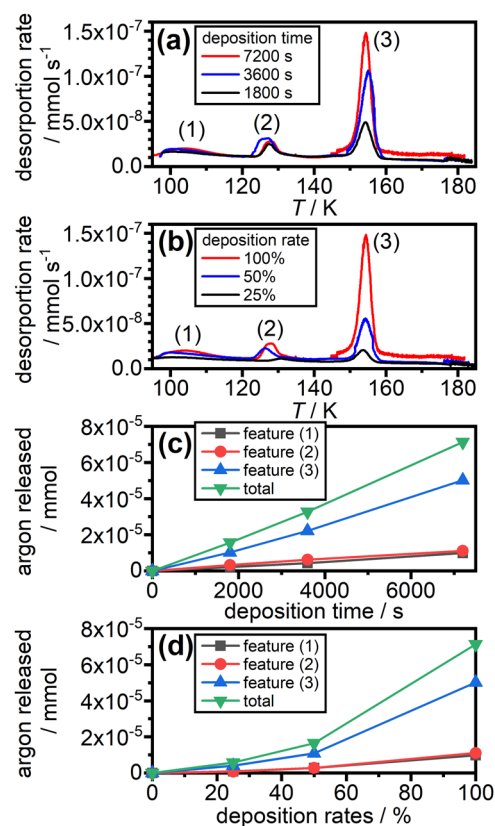

FIG. 6. Argon desorption rates for a variety of different deposition times and deposition rates. (a) TPD traces for different deposition times using 1.157×10^{-2} and 1.345×10^{-5} mmol s^{-1} as the deposition rates of water and argon, respectively. (b) TPD traces for 2-h deposition experiments using reduced deposition rates of both water and argon indicated as percentages of the rates used for panel (a). [(c) and (d)] Quantitative analyses of the amounts of released argon during the three desorption processes shown in (a) and (b).

proportionally reduced, there will be fewer water molecules locally available to trap a given argon atom. Consistent with this, the water to argon ratio in the deposits increases from 1 169 000:1 to 2 517 000:1 and 3 595 000:1 as the deposition rates are reduced by 50% and 25%, respectively (cf. Table S1). On balance, it seems as if reducing the deposition rates has more of an effect on the gas-trapping efficiency rather than on changing the morphology of the deposit. This view is supported by the fact that the relative amounts of argon released during the three desorption features remain roughly constant as the deposition rates are changed (cf. Table S1). In any case, it can be concluded that the three desorption features are robustly found with our experimental setup across a range of film thicknesses and deposition rates.

Increasing the amount of argon

To investigate how much argon can be immobilized within the 100 μm ASW films, the argon to water ratio was increased from 1:2460 to 1:860 and 1:5 while keeping the water leak rate constant

at 1.157×10^{-2} mmol s^{-1}. The corresponding TPD traces are shown in Fig. 7(a). It is interesting to note that the onset temperatures of desorption features (1) and (2) shift toward lower temperatures for the 1:5 ratio, suggesting that the increased local pressures of the argon now have an influence on the desorption temperatures. The onset temperature of process (3) does not seem to be affected by the argon concentration, which is consistent with the desorption of matrix-isolated argon upon crystallization.

Figure 7(b) shows the quantitative analysis of the recorded desorption features which illustrates that our earlier experiments were far away from the maximal solubility of argon in ASW. Unfortunately, the third desorption feature for the 1:5 ratio experiment could not be fully recorded because the pressure exceeded the permissible limit of our mass spectrometer. The ratio of the area of the third feature in the other two experiments with respect to the areas of the first and second feature is constant. Assuming that this would also be the case for the 1:5 ratio experiment, it can be estimated that the water to gas ratio in this deposit is 74 120:1 compared to 1 169 000:1 in our standard experiment (cf. Table S1).

Effect of baffling the gas flow into the chamber

In a final step, the effect of baffling on the three desorption features was investigated. Baffling the water-vapor beam has generally led to less porous ASW in previous studies.[21–23,63] As shown in Fig. 2(b), using the mesh on top of the gas-inlet tube already leads to some degrees of baffling. However, in order to investigate the effect of more substantially disrupting the gas flow into the vacuum chamber, a "standard" 1:860 Ar:H$_2$O codeposition experiment was carried out except that the gas flow into the chamber was blocked with a metal plate. As can be seen from Fig. 2(c), this severely disrupts the gas flow. A comparison of the water partial pressures recorded upon heating Ar@ASW either baffled with the mesh or blocked with a metal plate shows that the blocking leads to a smaller amount of deposit [cf. Fig. 8(a)] consistent with the QCM data shown in
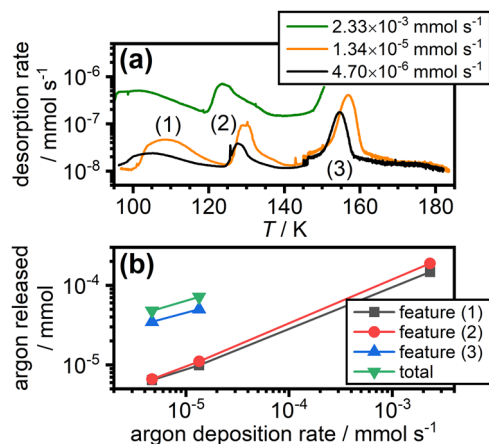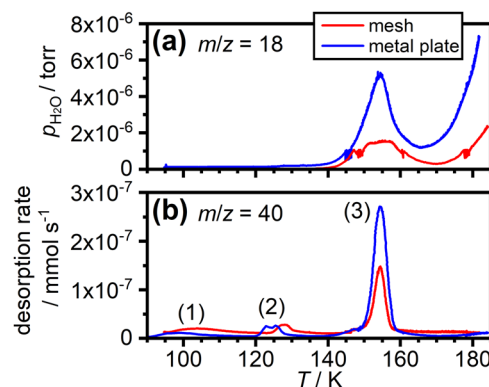

FIG. 8. (a) Partial pressures of water and (b) desorption rates of argon recorded after codeposition using either a mesh or a solid metal disk to baffle the gas flow into the vacuum chamber.

Fig. S4. Inspection of the argon desorption data shown in Fig. 8(b) reveals two significant differences. First, the low-temperature desorption feature (1) is much weaker for the "metal plate" experiment (cf. Table S1). This implies that background deposition conditions lead to ASW films with reduced amounts of open cracks. Second, the background deposition leads to significantly increased levels of matrix-isolated argon as indicated by the intense third desorption peak which is greater than the one observed for the corresponding "mesh" experiment. This is remarkable because it means that more matrix-isolated argon is present despite the overall lower amounts of ASW. Since we cannot necessarily assume that all water is deposited on the plate during the "metal plate" deposition, further quantifications are difficult. Nevertheless, it is clear that baffling the flow of the inlet gas, out of all the investigated experimental parameters, has had the most pronounced effect on the morphology of the ASW deposit. The more random fluxes of the background deposition decrease the amounts of open cracks but increase the amount of matrix-isolated argon.

CONCLUSIONS

Our study underpins once more the highly complex nature of ASW that arises from its structural heterogeneity across several length scales combined with the complicated dynamic behavior of the water molecules. Using argon as a gaseous "nanoprobe" in the 95–185 K temperature range, we have shown that two trapping environments exist in macroscopic ASW that are not present in nanoscale films. First, argon can be located in open cracks from which they can be removed by heating above ~100 K. If the ASW is created via background deposition, then these types of cracks appear to be reduced. Independent of the deposition geometry, argon is released in a second desorption process from internal voids at ~125 K. This process is thought to arise from the underlying orientational glass transition of ASW/LDA[34,35] which facilitates the collapse of these voids. The third desorption process, which has also been observed for nanoscale Ar@ASW,[43,45] is attributed to matrix-isolated argon that is liberated as the ASW crystallizes. In the case of background deposition, much more effective matrix-isolation is

FIG. 7. (a) Desorption rates of argon recorded upon heating after increasing the flow rates of argon during the codeposition from 4.70×10^{-6} to 1.34×10^{-5} and 2.33×10^{-3} mmol s^{-1}. (b) Quantitative analysis of the desorption features shown in (a).

observed. The assignment of the three desorption processes to the different local environments is supported by using methane, helium, and carbon dioxide as additional gaseous nanoprobes. Overall, it is clear that the morphology of ASW films becomes more complex as the thickness is increased from nanoscale films to the macroscopic deposits prepared in this study. Following the crossover from nanoscale films to thicker deposits and the appearance of the first two desorption features will be the focus of future studies.

In addition to the structural complexity of ASW, it is noted that the crystallization product, ice Isd, has recently been demonstrated to be a quite complex material as well. Different fractions of cubic/hexagonal stacking and even long-range memory effects within the stacking sequences are possible.[50,51,72–74] The exact details of the stacking disorder in ice Isd have been shown to affect its physical and chemical properties.[75–78] How and if structural differences present in ASW affect the details of the stacking disorder in ice Isd and hence its properties will need to be investigated in future studies including further studies into the complex changes in the QCM data around the crystallization.

SUPPLEMENTARY MATERIAL

See supplementary material for (1) details on the experimental approach for determining desorption rates, (2) the results from the quantitative analyses of all TPD data, (3) selected QCM deposition rates, (4) discussion of the QCM data, (5) Python code used for analyzing the QCM data, and (6) the TPD data after "bombarding" ASW with argon.

ACKNOWLEDGMENTS

REFERENCES

[1] C. G. Salzmann, J. Chem. Phys. **150**, 060901 (2019).

[2] M. Millot, F. Coppari, J. R. Rygg, A. Correa Barrios, S. Hamel, D. C. Swift, and J. H. Eggert, Nature **569**, 251 (2019).

[3] O. Mishima, L. D. Calvert, and E. Whalley, Nature **310**, 393 (1984).

[4] T. Loerting, C. Salzmann, I. Kohl, E. Mayer, and A. Hallbrucker, Phys. Chem. Chem. Phys. **3**, 5355 (2001).

[5] R. J. Nelmes, J. S. Loveday, T. Strässle, C. L. Bull, M. Guthrie, G. Hamel, and S. Klotz, Nat. Phys. **2**, 414 (2006).

[6] J. J. Shephard, S. Klotz, and C. G. Salzmann, J. Chem. Phys. **144**, 204502 (2016).

[7] A. G. G. M. Tielens, Rev. Mod. Phys. **85**, 1021 (2013).

[8] D. A. Williams, H. J. Fraser, and M. R. S. McCoustra, Astron. Geophys. **43**, 2.10 (2002).

[9] M. C. De Sanctis, F. Capaccioni, M. Ciarniello, G. Filacchione, M. Formisano, S. Mottola, A. Raponi, F. Tosi, D. Bockelee-Morvan, S. Erard, C. Leyrat, B. Schmitt, E. Ammannito, G. Arnold, M. A. Barucci, M. Combi, M. T. Capria, P. Cerroni, W. H. Ip, E. Kuehrt, T. B. McCord, E. Palomba, P. Beck, E. Quirico, and V. T. The, Nature **525**, 500 (2015).

[10] G. Filacchione, M. C. De Sanctis, F. Capaccioni, A. Raponi, F. Tosi, M. Ciarniello, P. Cerroni, G. Piccioni, M. T. Capria, E. Palomba, G. Bellucci, S. Erard, D. Bockelee-Morvan, C. Leyrat, G. Arnold, M. A. Barucci, M. Fulchignoni, B. Schmitt, E. Quirico, R. Jaumann, K. Stephan, A. Longobardo, V. Mennella, A. Migliorini, E. Ammannito, J. Benkhoff, J. P. Bibring, A. Blanco, M. I. Blecka, R. Carlson, U. Carsenty, L. Colangeli, M. Combes, M. Combi, J. Crovisier, P. Drossart, T. Encrenaz, C. Federico, U. Fink, S. Fonti, W. H. Ip, P. Irwin, E. Kuehrt, Y. Langevin, G. Magni, T. McCord, L. Moroz, S. Mottola, V. Orofino, U. Schade, F. Taylor, D. Tiphene, G. P. Tozzi, P. Beck, N. Biver, L. Bonal, J. P. Combe, D. Despan, E. Flamini, M. Formisano, S. Fornasier, A. Frigeri, D. Grassi, M. S. Gudipati, D. Kappel, F. Mancarella, K. Markus, F. Merlin, R. Orosei, G. Rinaldi, M. Cartacci, A. Cicchetti, S. Giuppi, Y. Hello, F. Henry, S. Jacquinod, J. M. Reess, R. Noschese, R. Politi, and G. Peter, Nature **529**, 368 (2016).

[11] Y. Oba, N. Miyauchi, H. Hidaka, T. Chigai, N. Watanabe, and A. Kouchi, Astrophys. J. **701**, 464 (2009).

[12] E. F. Burton and W. F. Oliver, Nature **135**, 505 (1935).

[13] E. F. Burton and W. F. Oliver, Proc. R. Soc. London, Ser. A **153**, 166 (1935).

[14] P. Jenniskens and D. F. Blake, Science **265**, 753 (1994).

[15] A. H. Narten, C. G. Venkatesh, and S. A. Rice, J. Chem. Phys. **64**, 1106 (1976).

[16] P. Jenniskens, D. F. Blake, M. A. Wilson, and A. Pohorille, Astrophys. J. **455**, 389 (1995).

[17] D. S. Olander and S. A. Rice, Proc. Natl. Acad. Sci. U. S. A. **69**, 98 (1972).

[18] R. S. Smith, N. G. Petrik, G. A. Kimmel, and B. D. Kay, Acc. Chem. Res. **45**, 33 (2012).

[19] B. J. Murray and E. J. Jensen, J. Atmos. Sol.-Terr. Phys. **72**, 51 (2010).

[20] D. T. Bowron, J. L. Finney, A. Hallbrucker, I. Kohl, T. Loerting, and A. K. Soper, J. Chem. Phys. **125**, 194502 (2006).

[21] E. Mayer and R. Pletzer, J. Chem. Phys. **80**, 2939 (1984).

[22] E. Mayer and R. Pletzer, Nature **319**, 298 (1986).

[23] E. Mayer and R. Pletzer, J. Phys. Colloq. **48**, 581 (1987).

[24] K. P. Stevenson, G. A. Kimmel, Z. Dohnalek, R. S. Smith, and B. D. Kay, Science **283**, 1505 (1999).

[25] G. A. Kimmel, K. P. Stevenson, Z. Dohnálek, R. S. Smith, and B. D. Kay, J. Chem. Phys. **114**, 5284 (2001).

[26] Z. Dohnálek, G. A. Kimmel, P. Ayotte, R. S. Smith, and B. D. Kay, J. Chem. Phys. **118**, 364 (2002).

[27] R. S. Smith, T. Zubkov, Z. Dohnálek, and B. D. Kay, J. Phys. Chem. B **113**, 4000 (2009).

[28] E. Mayer and A. Hallbrucker, J. Am. Chem. Soc. **12**, 749 (1989).

[29] G. P. Johari, A. Hallbrucker, and E. Mayer, J. Chem. Phys. **95**, 2955 (1991).

[30] B. Rowland, M. Fisher, and J. P. Devlin, J. Chem. Phys. **95**, 1378 (1991).

[31] J. J. Shephard, J. S. O. Evans, and C. G. Salzmann, J. Phys. Chem. Lett. **4**, 3672 (2013).

[32] J. A. McMillan and S. C. Los, Nature **206**, 806 (1965).

[33] A. Hallbrucker, E. Mayer, and G. P. Johari, J. Phys. Chem. **93**, 4986 (1989).

[34] M. Fisher and J. P. Devlin, J. Phys. Chem. **99**, 11584 (1995).

[35] J. J. Shephard and C. G. Salzmann, J. Phys. Chem. Lett. **7**, 2281 (2016).

[36] C. R. Hill, C. Mitterdorfer, T. G. A. Youngs, D. T. Bowron, H. J. Fraser, and T. Loerting, Phys. Rev. Lett. **116**, 215501 (2016).

[37] J. Swenson, Phys. Chem. Chem. Phys. **20**, 30095 (2018).

[38] F. Perakis, K. Amann-Winkel, F. Lehmkühler, M. Sprung, D. Mariedahl, J. A. Sellberg, H. Pathak, A. Späh, F. Cavalca, D. Schlesinger, A. Ricci, A. Jain, B. Massani, F. Aubree, C. J. Benmore, T. Loerting, G. Grübel, L. G. M. Pettersson, and A. Nilsson, Proc. Natl. Acad. Sci. U. S. A. **114**, 8193 (2017).

[39] Y. Xu, N. G. Petrik, R. S. Smith, B. D. Kay, and G. A. Kimmel, Proc. Natl. Acad. Sci. U. S. A. **113**, 14921 (2016).

[40] C. R. Kwang-Hua, Physica A **519**, 18 (2019).

[41] S. M. McClure, D. J. Safarik, T. M. Truskett, and C. B. Mullins, J. Phys. Chem. B **110**, 11033 (2006).

[42] M. D. Ediger, J. Chem. Phys. **147**, 210901 (2017).

[43] P. Ayotte, R. S. Smith, K. P. Stevenson, Z. Dohnálek, G. A. Kimmel, and B. D. Kay, J. Geophys. Res. Planets **106**, 33387, https://doi.org/10.1029/2000je001362 (2001).

[44] R. A. May, R. S. Smith, and B. D. Kay, J. Chem. Phys. **138**, 104501 (2013).

[45] A. Bar-Nun, G. Notesco, and T. Owen, Icarus **190**, 655 (2007).

[46] G. Notesco, A. Bar-Nun, and T. Owen, Icarus **162**, 183 (2003).

[47] G. Sauerbrey, Z. Phys. **155**, 206 (1959).

[48] D. Johannsmann, Phys. Chem. Chem. Phys. **10**, 4516 (2008).

[49] L. G. Dowell and A. P. Rinfret, Nature **188**, 1144 (1960).

[50] W. F. Kuhs, C. Sippel, A. Falentya, and T. C. Hansen, Proc. Natl. Acad. Sci. U. S. A. **109**, 21259 (2012).

[51] T. L. Malkin, B. J. Murray, C. G. Salzmann, V. Molinero, S. J. Pickering, and T. F. Whale, Phys. Chem. Chem. Phys. **17**, 60 (2015).

[52] D. Johannsmann, *The Quartz Crystal Microbalance in Soft Matter Research* (Springer International Publishing, 2015).

[53] A. K. Srivastava and P. Sakthivel, J. Vac. Sci. Technol. A **19**, 97 (2001).

[54] T. Loerting, K. Winkel, M. Seidl, M. Bauer, C. Mitterdorfer, P. H. Handle, C. G. Salzmann, E. Mayer, J. L. Finney, and D. T. Bowron, Phys. Chem. Chem. Phys. **13**, 8783 (2011).

[55] A. Kouchi, Nature **330**, 550 (1987).

[56] M. Nachbar, D. Duft, and T. Leisner, J. Phys. Chem. B **122**, 10044 (2018).

[57] R. S. Smith, C. Huang, E. K. L. Wong, and B. D. Kay, Phys. Rev. Lett. **79**, 909 (1997).

[58] R. S. Smith, R. A. May, and B. D. Kay, J. Phys. Chem. B **120**, 1979 (2016).

[59] A. Bar-Nun, I. Kleinfeld, and E. Kochavi, Phys. Rev. B **38**, 7749 (1988).

[60] J. H. E. Cartwright, B. Escribano, and C. I. Sainz-Díaz, Thin Solid Films **518**, 3422 (2010).

[61] E. Lisitsin-Baranovsky, S. Delage, O. Sucre, O. Ofer, P. Ayotte, and G. Alexandrowicz, J. Phys. Chem. C **120**, 25445 (2016).

[62] C. Bu, C. A. Dukes, and R. A. Baragiola, Appl. Phys. Lett. **109**, 201902 (2016).

[63] C. Mitterdorfer, M. Bauer, T. G. A. Youngs, D. T. Bowron, C. R. Hill, H. J. Fraser, J. L. Finney, and T. Loerting, Phys. Chem. Chem. Phys. **16**, 16013 (2014).

[64] T. Zubkov, R. S. Smith, T. R. Engstrom, and B. D. Kay, J. Chem. Phys. **127**, 184707 (2007).

[65] T. Zubkov, R. S. Smith, T. R. Engstrom, and B. D. Kay, J. Chem. Phys. **127**, 184708 (2007).

[66] M. Minissale, E. Congiu, and F. Dulieu, Astron. Astrophys. **585**, A146 (2016).

[67] M. P. Collings, M. A. Anderson, R. Chen, J. W. Dever, S. Viti, D. A. Williams, and M. R. S. McCoustra, Mon. Not. R. Astron. Soc. **354**, 1133 (2004).

[68] S. Malyk, G. Kumi, H. Reisler, and C. Wittig, J. Phys. Chem. A **111**, 13365 (2007).

[69] L. Edridge John, K. Freimann, J. Burke Daren, and A. Brown Wendy, Philos. Trans. R. Soc., A **371**, 20110578 (2013).

[70] J. He, S. M. Emtiaz, A. Boogert, and G. Vidali, Astrophys. J. **869**, 41 (2018).

[71] K. Isokoski, J. B. Bossa, T. Triemstra, and H. Linnartz, Phys. Chem. Chem. Phys. **16**, 3456 (2014).

[72] T. C. Hansen, M. M. Koza, and W. F. Kuhs, J. Phys.: Condens. Matter **20**, 285104 (2008).

[73] T. L. Malkin, B. J. Murray, A. V. Brukhno, J. Anwar, and C. G. Salzmann, Proc. Natl. Acad. Sci. U. S. A. **109**, 1041 (2012).

[74] C. G. Salzmann, B. J. Murray, and J. J. Shephard, Diamond Relat. Mater. **59**, 69 (2015).

[75] J. E. Shilling, M. A. Tolbert, O. B. Toon, E. J. Jensen, and B. J. Murray, Geophys. Res. Lett. **33**, L17801, https://doi.org/10.1029/2006gl026671 (2006).

[76] B. J. Murray, C. G. Salzmann, A. J. Heymsfield, S. Dobbie, R. R. Neely, and C. J. Cox, Bull. Am. Meteorol. Soc. **96**, 1519 (2015).

[77] T. H. G. Carr, J. J. Shephard, and C. G. Salzmann, J. Phys. Chem. Lett. **5**, 2469 (2014).

[78] P. Behr, A. Terziyski, and R. Zellner, J. Phys. Chem. A **110**, 8098 (2006).